Well-crystallized α-FeOOH cocatalysts modified $BiVO_4$ photoanodes for efficient and stable photoelectrochemical water splitting

Wen Zhang[a], Jiani Ma[a], Lunqiao Xiong[b], Hai-Ying Jiang*[a] and Junwang Tang*[b]

[a] *Key Laboratory of Synthetic and Natural Functional Molecule of the Ministry of Education, The Energy and Catalysis Hub, College of Chemistry and Materials Science, Northwest University, Xi'an 710127, P. R. China.*

[b] *Department of Chemical Engineering, University College London, Torrington Place, London WC1E 7JE, U.K.*

* Corresponding author

E-mail: jianghy@nwu.edu.cn (H. Jiang)

E-mail: junwang.tang@ucl.ac.uk (J. Tang)

ABSTRACT

Monoclinic bismuth vanadate ($BiVO_4$) is a potential photoanode for photoelectrochemical (PEC) water splitting, but it suffers from poor electron-hole separation. Here, a reproducible chemical bath deposition method was employed to immobilize well-crystalized α-FeOOH on the $BiVO_4$ photoanode, resulting into a nearly unity faradaic efficiency and more than 21-fold higher solar to fuel conversion efficiency compared with pure $BiVO_4$ photoanode. The precursor containing Fe^{2+} ions has been identified to be crucial for preparation of this well-crystallized α-FeOOH cocatalyst. Systematic studies revealed that the high efficiency and excellent stability of α-FeOOH(P-II)/$BiVO_4$ photoanode were attributed to the well-crystallized α-FeOOH that facilitated the charge carrier separation and transfer for PEC water splitting. Our findings thus not only demonstrated a highly stable and efficient photoanode for PEC water splitting, but also provided a promising strategy for the rational design of well-crystallized α-FeOOH.

KEYWORDS: crystallized α-FeOOH, $BiVO_4$, photoanode, stability, water splitting.

■ INTRODUCTION

Photoelectrochemical (PEC) water splitting has emerged as a promising pathway for converting solar energy into sustainable hydrogen fuels. One of the key challenges in PEC water splitting is to accelerate the oxygen evolution reaction (OER), the rate-limiting step with a four-electron process, which occurs at the interface of a photoanode and electrolyte.[1-3] Up to now, monoclinic bismuth vanadate ($BiVO_4$) has been regarded as an ideal photoanode in PEC water splitting, due to its unique features of suitable bandgap energy, favorable band-edge position, non-toxicity as well as earth-abundance. Nevertheless, the reported photocurrents of pure $BiVO_4$ photoanodes are much lower than its theoretical expectation of 7.5 mA cm^{-2} (AM 1.5 G, 100 mW cm^{-2}), suffering from poor electron-hole separation and sluggish oxygen evolution reaction.[4-7] To handle these issues, a proper oxygen evolution cocatalyst (OEC) is crucial to improve the PEC activity of $BiVO_4$ by enhancing the electron-hole separation and facilitating the O_2 evolution kinetics.[8-12]

Among various cocatalysts, p-type VIII metal oxy-hydroxides, extensively used as electrocatalysts for OER, are particularly attractive because of their high efficiency and low cost.[13-17] Previous studies demonstrated that loading FeOOH,[18,19] NiOOH[20] or CoOOH[21] cocatalyst on $BiVO_4$ photoanodes can effectively improve the O_2 evolution kinetics. Also, Choi *et al.*[22] suggested that FeOOH is indeed more effective than the others to reduce the interface recombination of photocarriers for the OECs/$BiVO_4$ junction compared with that of NiOOH, which has stimulated the majority of studies on FeOOH. As known, electro-deposition and photo-deposition are widely used for

loading FeOOH layer on $BiVO_4$ photoanodes. Note that the obtained FeOOH catalysts generally possess an amorphous structure and highly unstable in alkaline electrolytes at a high anodic potential.[23-25] Recently, chemical bath deposition (CBD) method, owing to its simplicity, convenience and low-cost, has attracted considerable attention for the deposition of metal oxy-hydroxides thin films.[26,27] In our previous research, we synthesized α-FeOOH by the CBD method and found that the crystalline α-FeOOH electrocatalyst was much more stable than amorphous FeOOH in alkali solution, without compromising the catalytic performance.[28] In terms of practical application, finding a rational approach to design an efficient and stable FeOOH cocatalyst is crucial. Building on the successful study of the crystalline α-FeOOH as electrocatalyst, to immobilize the highly crystallized α-FeOOH on $BiVO_4$ photoanode would be a promising approach for constructing a high performance and stable PEC photoanode.

In this study, we present an efficient chemical bath deposition method for growing well-crystallized α-FeOOH layer with high stability for PEC water splitting. To obtain the high performance of α-FeOOH/$BiVO_4$ photoanodes, $BiVO_4$ films were treated with different $FeCl_x$ precursor solutions, including $FeCl_2$, $FeCl_3$ and their mixture ($FeCl_2$/$FeCl_3$) to immobilize the stable OER cocatalysts. After loading α-FeOOH on $BiVO_4$, all samples showed an increased photocurrent compared with pure $BiVO_4$. The synthesized crystalline α-FeOOH(P-II)/$BiVO_4$ photoanode exhibited the highest photocurrent density of 2.64 mA cm^{-2} at 1.23 V *vs.* RHE, nearly 1.5-fold higher than that of amorphous FeOOH(P-III)/$BiVO_4$ and even 8-fold higher than that of pristine $BiVO_4$ (0.35 mA cm^{-2}). Remarkably, stable PEC water splitting of crystalline

FeOOH(P-II)/$BiVO_4$ photoanode could be achieved for over 20 hours without any obvious decay. The reason behind this enhanced performance was then discussed.

■ EXPERIMENTAL SECTION

Preparation of different α-FeOOH/$BiVO_4$ photoanodes. $BiVO_4$ photoanodes were prepared by referring to the previous research reported by Choi and coworkers.[22] Different α-FeOOH modified $BiVO_4$ photoanodes were synthesized by a facile chemical bath deposition method, as illustrated in Scheme 1. Three different reaction solutions, including $FeCl_2$ (0.02 M), $FeCl_3$ (0.02 M) and their mixture (0.01 M $FeCl_2$ and 0.01 M $FeCl_3$), were selected as Fe source. Before impregnation, the pH values of solutions were adjusted to 3.42 by adding 1 M NaOH or HCl. Then, the obtained $BiVO_4$ photoanodes were treated with different $FeCl_x$ as the reaction precursor for 24 h at room temperature. The resultant electrodes were denoted as α-FeOOH(P-II)/$BiVO_4$, α-FeOOH(P-III)/$BiVO_4$ and α-FeOOH(P-II/III)/$BiVO_4$, correspondingly.

To optimize the photoanodes, the different α-FeOOH/$BiVO_4$ photoanodes were also prepared in solutions with different pH values (Table S2) and impregnation time (16 h, 24 h, 36 h).

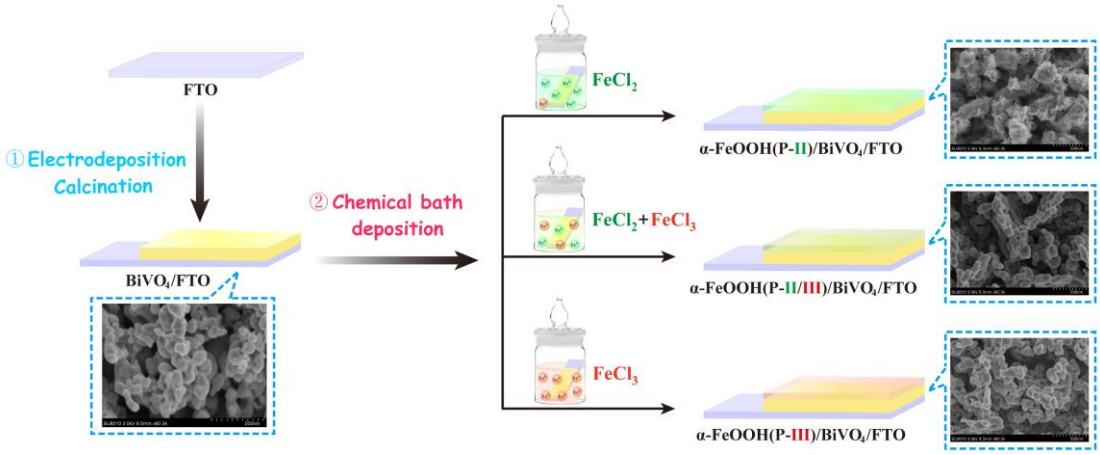

Scheme 1. Schematic illustration of the fabrication procedure and corresponding SEM images of the $BiVO_4$, α-FeOOH(P-II)/$BiVO_4$, α-FeOOH(P-II/III)/$BiVO_4$ and α-FeOOH(P-III)/$BiVO_4$ photoanodes.

Characterization. Scanning electron microscopy (SEM, Hitachi SU8010) was used to investigate the morphologies of the as-prepared samples. The chemical compositions, morphologies and nanostructures of the samples were characterized by high-resolution transmission electron microscopy (HR-TEM, FEI Tecnai G2 S-Twin F20). X-ray diffraction (XRD) patterns were performed on Bruker AXS-D8 diffractometer by using Cu Kα radiation (λ = 0.15418 nm) with the 2θ range from 10° to 80° at a scanning rate of 0.1° s^{-1}. X-ray photoelectron spectroscopy (XPS) was carried out by using a PHI5000 VersaProbeIII XPS spectrometer. The binding energy of the spectrometer was calibrated by using the C1s peak at the position of 284.6 eV. ICP-MS (Agilent 7900 ICP-MS) was employed to analyses the elemental composition of the samples. UV-vis diffuse reflectance spectra were executed on UV-vis spectrometer (UV-2401PC, Shimadzu) equipped with integrated sphere method and employed $BaSO_4$ as the reflectance standard reference. Fourier-transform infrared spectroscopy (FT-IR) (Nicolet 6700, Thermo Fisher) was employed to study the chemical bonds of the prepared samples. Raman spectra were obtained from Renishaw Ramascope (Confocal Raman Microscope, Renishaw, Gloucester-shire, U.K.) with a He-Ne laser (λ = 532 nm).

PEC measurements. PEC performance measurements were carried out by employing a CHI660E electrochemical workstation (CH Instruments, Shanghai, China) with a typical three-electrode arrangement. The as-obtained α-FeOOH/$BiVO_4$,

Ag/AgCl (saturated KCl) and a platinum foil (1 cm×1 cm) were used as the working, reference and counter electrodes, respectively. The simulated solar illumination was obtained by the light from a Xe 300 W lamp through an AM 1.5 G filter and the light intensity was carefully calibrated to 100 mW cm^{-2} by a thermopile optical detector (Newport, Model 818P-040-25). Samples were illuminated from the back side (FTO substrate side), and the illuminated areas were 1.2 cm^2. 0.2 M Na_2SO_4 solution (pH 7) was used as the electrolyte for all PEC measurements. Photocurrent-potential curves were obtained using linear sweep voltammogram (LSV) in a voltage window of -0.4 V~1.1 V *vs*. Ag/AgCl with a scan rate of 10 mV s^{-1}. All the potentials *vs*. RHE were converted from the potentials *vs*. Ag/AgCl according to the Nernst equation:

$$E_{\mathrm{RHE}} = E_{\mathrm{Ag/AgCl}} + 0.059\ \mathrm{pH} + E^{\theta}_{\mathrm{Ag/AgCl}}$$

Where E_{RHE} refers to the converted potential *vs.* RHE. $E_{\mathrm{Ag/AgCl}}$ is the experimentally measured potential and $E^{\theta}_{\mathrm{Ag/AgCl}}$ = 0.209 V (*vs.* Ag/AgCl) at 25 °C.

Incident-photon-to-current conversion efficiency (IPCE) was obtained using an Oriel Cornerstone 260 1/4 m monochromator coupled with a 300 W Xe arc lamp passed through an AM 1.5G filter as the simulated light source. IPCE was measured at 1.23 V *vs*. RHE in 0.2 M Na_2SO_4 solution using the three-electrode system described above for PEC measurements. IPCE values were calculated as follow:

$$\mathrm{IPCE}(\%) = \frac{1240 \times J\ (\mathrm{mA\ cm^{-2}})}{P_{\mathrm{light}}\ (\mathrm{mW\ cm^{-2}}) \times \lambda\ (\mathrm{nm})} \times 100$$

Where J presents the photocurrent density obtained from the electrochemical workstation, λ is the wavelength of incident light, and P_{light} is the measured light power density at that wavelength.

Supposing 100% faradaic efficiency, applied bias photon-to-current efficiency (ABPE) can be calculated using the following equation:

$$\text{ABPE (\%)} = \frac{J\,(\text{mA cm}^{-2}) \times (1.23\text{-}V_{\text{bias}})}{P_{\text{light}}\,(\text{mW cm}^{-2})} \times 100$$

Where J is the photocurrent density obtained from the electrochemical workstation. V_{bias} refers to the applied bias *vs* RHE (V), P_{light} is the total light intensity of AM 1.5 G (100 mV cm^{-2}). Electrochemical impedance spectroscopy (EIS) was recorded with an AC voltage amplitude of 10 mV at the open circuit potentials of the films under AM 1.5 G illumination (frequency range: 0.01 Hz~100 kHz).

Photoelectrochemical H_2 and O_2 evolution were measured using a two-electrode system (working electrode and the counter electrode) in an airtight single cell with a bias of 0.9 V in 0.2 M Na_2SO_4 solution (pH 7). H_2 and O_2 evolution were analyzed according to the standard H_2 or O_2 evolution curve by a gas chromatograph (SP-3420A, Beifen-Ruili). The amount of gas was determined by taking 100 μL of gas from the headspace of the cell and injecting it into a gas chromatograph every ten minutes.

■ RESULTS AND DISCUSSION

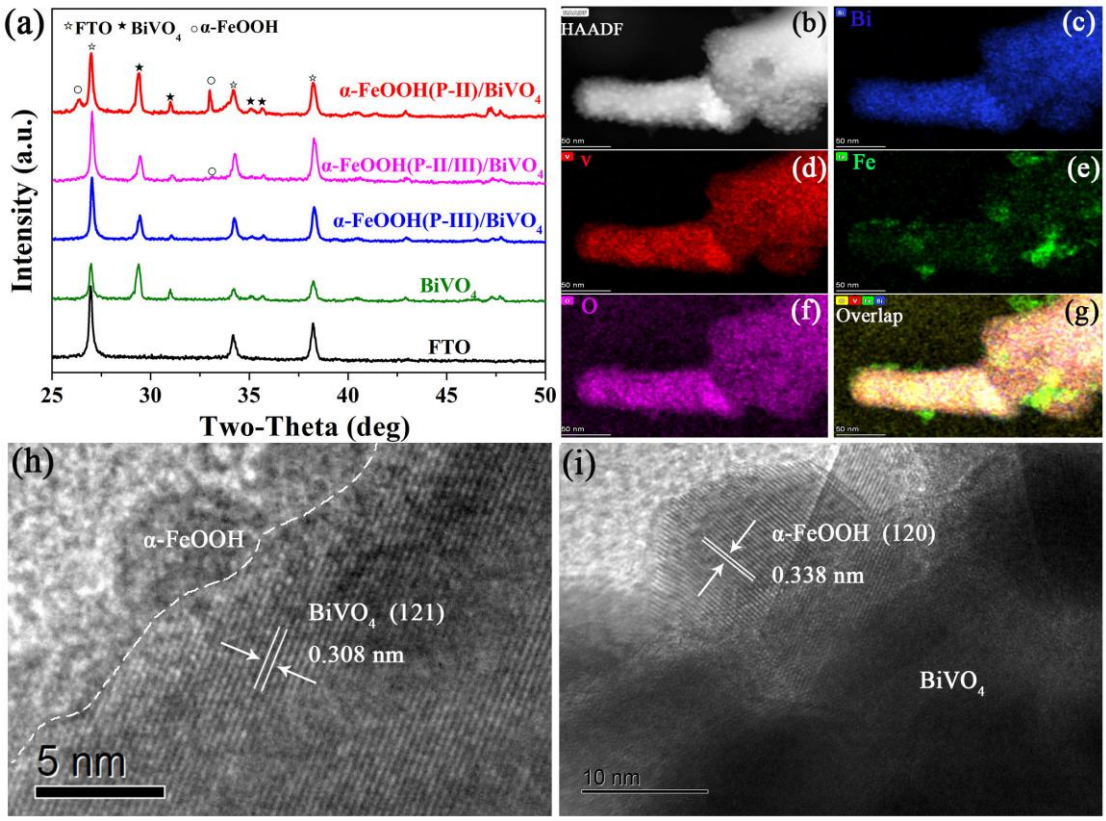

Figure 1. (a) XRD patterns of α-FeOOH(P-II)/$BiVO_4$ (red), α-FeOOH(P-II/III)/$BiVO_4$ (magenta), α-FeOOH(P-III)/$BiVO_4$ (blue) and $BiVO_4$ (olive) photoanodes. (b) HAADF and corresponding EDS elemental mapping images of (c) Bi, (d) V, (e) Fe, (f) O and (g) overlapping elements, respectively. (h and i) HR-TEM images of α-FeOOH(P-II)/$BiVO_4$.

The crystalline phase structures and chemical compositions of pristine $BiVO_4$ and as-synthesized three α-FeOOH/$BiVO_4$ samples were characterized by XRD first. It can be seen in Figure 1a, all peaks could be well indexed to monoclinic $BiVO_4$ (JCPDS No.14-0688) and FTO, demonstrating that the crystal structure of $BiVO_4$ is not affected by immobilization of α-FeOOH *via* chemical bath deposition. Upon impregnation of $FeCl_2$ on $BiVO_4$ (α-FeOOH(P-II)/$BiVO_4$), two evident characteristic peaks with 2θ values of 26.3° and 33.2° were detected in XRD pattern, which matches well with the (120) and (130) crystal planes of the standard crystalline phase of α-FeOOH (JCPDS No. 29-0713). It clearly reveals the formation of well-crystallized α-FeOOH on the

surface of $BiVO_4$ photoanode. In contrast, after impregnating $BiVO_4$ in mixture of $FeCl_2$ and $FeCl_3$ precursor solution, only a weak diffraction peak (33.2°) can be found in XRD pattern. When impregnating $BiVO_4$ in $FeCl_3$ solution, the diffraction peaks of α-FeOOH can be hardly observed. The decrease in the intensity of (120) and (130) for α-FeOOH supports the fact that $FeCl_2$ instead of $FeCl_3$ as the reaction precursor is beneficial to grow well-crystallized α-FeOOH.

To further investigate morphology and distribution of the prepared samples, SEM, HR-TEM, HAADF and corresponding EDS elemental mappings for α-FeOOH(P-II)/$BiVO_4$ photoanodes were carried out. The typical top-view SEM image of $BiVO_4$ is shown in Scheme 1. Compared with pristine $BiVO_4$, no evident morphological changes are observed after immobilizing α-FeOOH on $BiVO_4$, which may be due to the relatively low amount and ultrathin thickness of α-FeOOH nanolayers. Figure 1 (b-g) display that iron element in α-FeOOH(P-II)/$BiVO_4$ is well distributed in the whole regions, implying the uniform dispersion of α-FeOOH nanolayers on $BiVO_4$. HR-TEM image of α-FeOOH(P-II)/$BiVO_4$ (Figure 1h) clearly reveals that α-FeOOH nanolayer with a thickness of ~3 nm is tightly attached on the surface of $BiVO_4$. More importantly, the HR-TEM image in Figure 1(i) indicates the fringe spacing of 0.338 nm, which well agrees with the (120) lattice plan spacing of α-FeOOH in XRD pattern (Figure 1a), thus confirming the formation of α-FeOOH on $BiVO_4$. Moreover, according to the elemental mappings of α-FeOOH(P-II/III)/$BiVO_4$, α-FeOOH(P-III)/$BiVO_4$ in Figure S1a and Figure S1d, there are an even distribution of iron elements on the $BiVO_4$ surface after being prepared in the mixture of $FeCl_2$/$FeCl_3$ or $FeCl_3$ solution. However, we cannot observe the lattice fringes of α-FeOOH in α-FeOOH(P-II/III)/$BiVO_4$ and α-FeOOH(P-

III)/$BiVO_4$ samples (Figure S1) due to the low crystallinity or amorphous of α-FeOOH, which is consistent with the lattice observations in the XRD patterns (Figure 1a). Therefore, combining the results of XRD analysis, SEM and HR-TEM images, it adequately confirms that using $FeCl_2$ as the Fe precursor is more beneficial to grow α-FeOOH with the high crystallinity on the surface of $BiVO_4$.

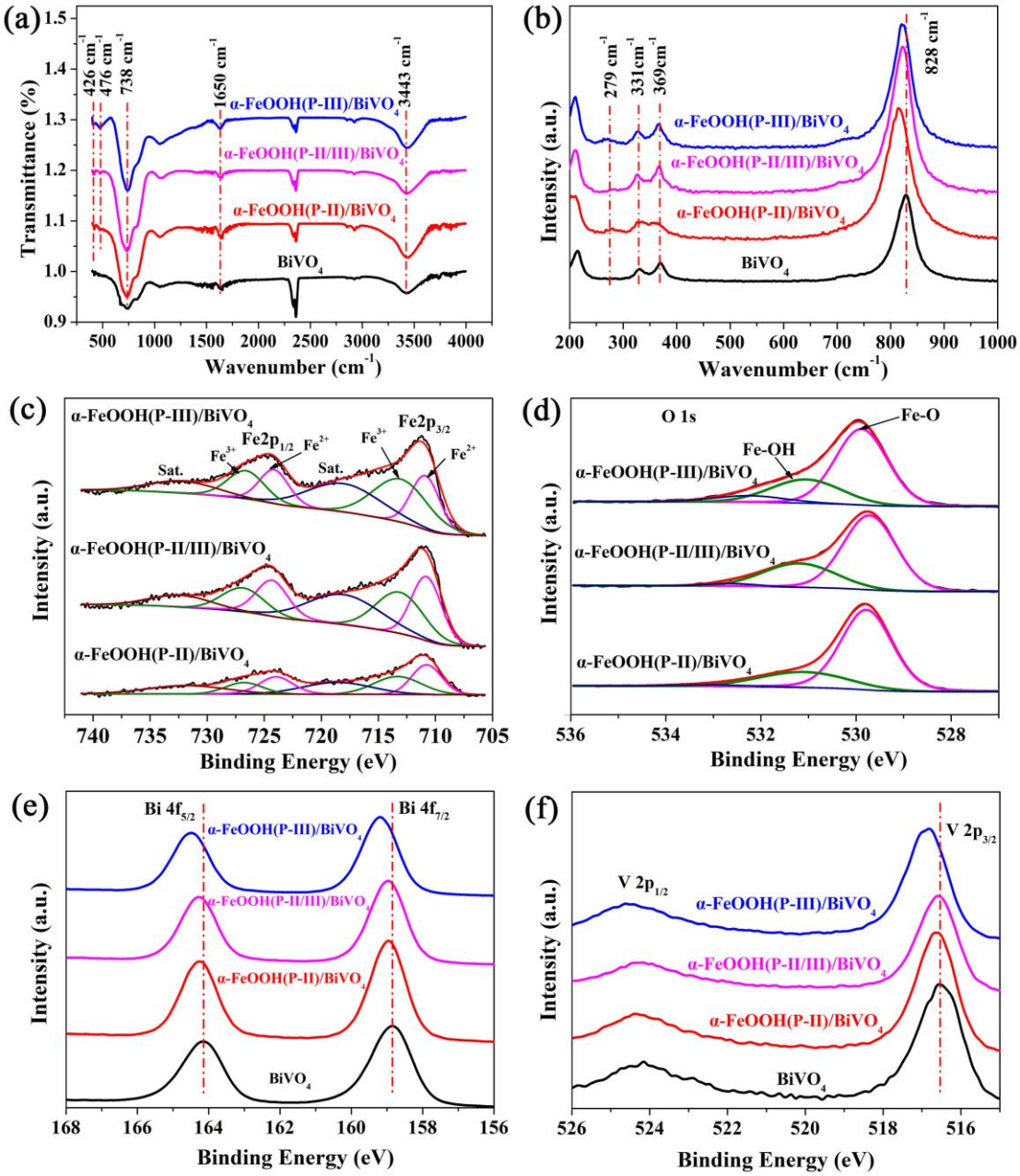

Figure 2. (a) FTIR and (b) Raman spectra of $BiVO_4$, α-FeOOH(P-III)/$BiVO_4$, α-FeOOH(P-II/III)/$BiVO_4$ and α-FeOOH(P-II)/$BiVO_4$. XPS high-resolution spectra of (c) Fe2p, (d) O 1s, (e) Bi

4f and (f) V 4f for different photoanodes.

To verify the presence of α-FeOOH on the surface of $BiVO_4$, FT-IR and Raman spectra were also observed. Figure 2a illustrates the FT-IR spectra of the as-prepared samples. For pure $BiVO_4$ sample (black line), a broad peak at ~3443 cm^{-1} is ascribed to the stretching vibration of O-H bond from the physically adsorbed water, and the sharp peak at 738 cm^{-1} is attributed to the symmetrical stretching vibration of the Bi-O bond. Compared with $BiVO_4$, three as-prepared α-FeOOH/$BiVO_4$ photoanodes show much stronger absorption peak at ~3443 cm^{-1}. The increased absorption band at around ~3443 cm^{-1} should be ascribed to the stretching vibration of O-H band from α-FeOOH. Typically, the peaks at 426 and 476 cm^{-1} in as-prepared α-FeOOH/$BiVO_4$ photoanodes can be assigned to Fe-O vibrational mode,[29,30] which implies that the α-FeOOH could be successfully immobilized on $BiVO_4$. To further confirm this conclusion, Raman spectroscopy was also acquired. Raman spectrum of the pristine $BiVO_4$ is shown in Figure 2b (black line), the peak at 828 cm^{-1} belongs to V-O symmetric stretching vibrations, and the peaks at 369 cm^{-1} and 331 cm^{-1} are interpreted as VO_4^{3-} symmetric bending vibrations. The characteristic peaks above match well with the bands of $BiVO_4$.[21] Notably, the as-prepared α-FeOOH/$BiVO_4$ photoanodes have typical peaks at ~279 cm^{-1}, which can be assigned to the Fe-O bending vibrations.[31,32] Compared with $BiVO_4$, the obtained α-FeOOH/$BiVO_4$ photoanodes show negatively shifted and broadened peaks for V-O symmetric stretching vibrations (828 cm^{-1}) and VO_4^{3-} symmetric bending vibrations (369 cm^{-1} and 331 cm^{-1}). Importantly, α-FeOOH(P-II)/$BiVO_4$ photoanode exhibits significant broadening of various VO_4^{3-} deformation

modes. These results clearly reveal that crystalline α-FeOOH could affect the local coordination of V in the bulk $BiVO_4$ sample.

To investigate the chemical states of Fe, the as-obtained photoanodes were studied by high-resolution Fe2p XPS spectra, as shown in Figure 2c, which confirms that both Fe^{2+} and Fe^{3+} exist in all samples while α-FeOOH(P-III)/$BiVO_4$ sample has highest amount of Fe^{3+}. Furthermore, ICP-MS measurements (Table S1) indicate that the Fe loading are 1.64 μg cm^{-2} and 1.87 μg cm^{-2} in α-FeOOH(P-II)/$BiVO_4$ and α-FeOOH(P-III)/$BiVO_4$ photoanode, respectively. Based on the XRD, HR-TEM, FTIR and Raman spectra one can make a conclusion that some iron ions exist in crystalline structure and the other in amorphous structure. Meanwhile, the high-resolution XPS spectra of O 1s in the three samples are also shown in Figure 2d. Two peaks at the binding energy of 529.8 eV and 531.3 eV can be assigned to Fe-O and Fe-OH bonds, respectively.[33] Furthermore, XPS spectra also reveal that the Bi 4f (Figure 2e) and V 2p (Figure 2f) peaks of three α-FeOOH/$BiVO_4$ samples are shifted to higher binding energy. For a metal atom, the XPS binding energy is proportional to the density of outer electrons.[34] When $BiVO_4$ is combined with α-FeOOH, the balance of the Fermi level between $BiVO_4$ and α-FeOOH is formed by electron transfer from $BiVO_4$ to Fe, resulting in decreased electron densities of Bi and V. More Fe^{3+} ions, more shift of the XPS spectra, indicating highest amount of Fe^{3+} in the sample of α-FeOOH(P-III)/$BiVO_4$ although they are in amorphous structure, consistent with the XPS analysis of Fe ions. Based on the observation above, it is reasonable to state that α-FeOOH nanolayers are successfully immobilized on $BiVO_4$ while only crystalline α-FeOOH was obtained

when using $FeCl_2$ as the precursor. The α-FeOOH(P-III)/$BiVO_4$ has a higher Fe content as indicated by both ICP-MS and XPS but with an amorphous structure, which is believe due to the different reaction pathway, *eg.* α-FeOOH(P-III)/$BiVO_4$ by a hydrolysis process of Fe^{3+} and α-FeOOH(P-II)/$BiVO_4$ by a very slow oxidation process. The latter process operated at room temperature provides a feasible route for crystalline FeOOH synthesis with small particles size.

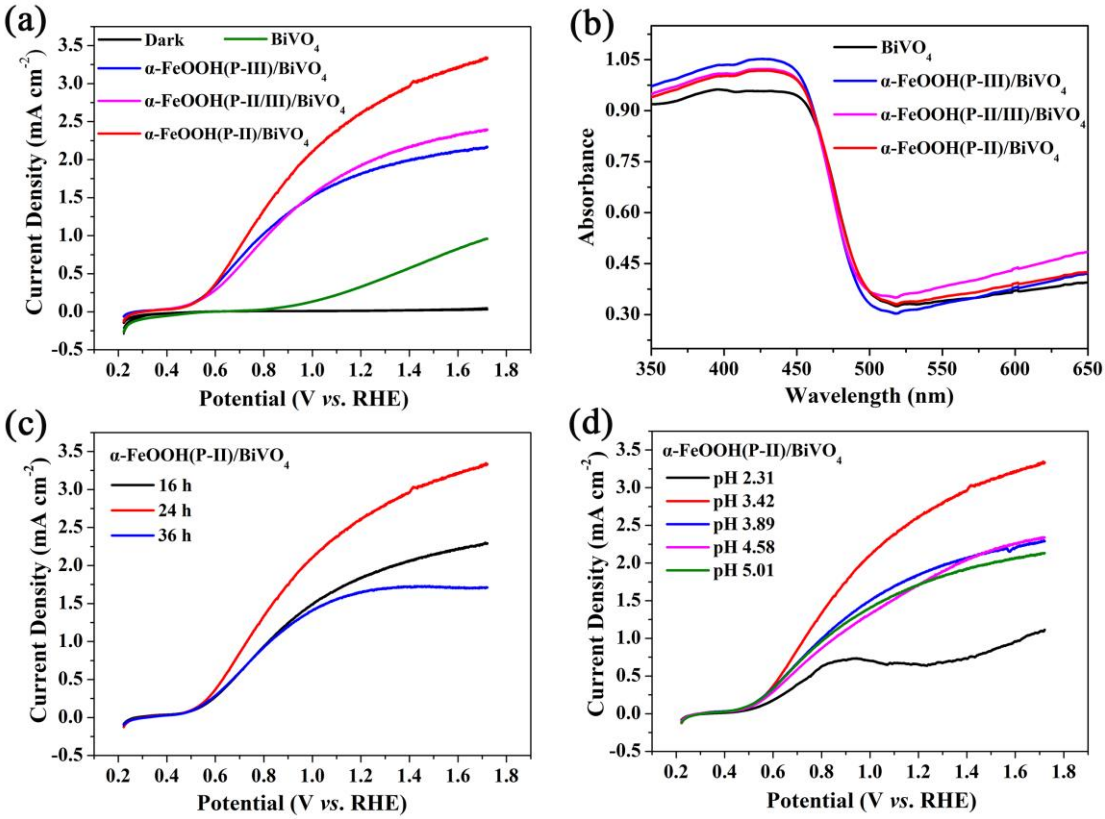

Figure 3. (a) *J-V* curves measured with 0.2 M Na_2SO_4 (pH = 7) under dark (black line) or AM 1.5G (100 mW cm^{-2}) illumination at a scan rate of 10 mV s^{-1}. (b) UV-vis absorbance spectra of different photoanodes. (c) α-FeOOH(P-II)/$BiVO_4$ photoanode prepared by 0.02 M $FeCl_2$ (pH = 3.42) for 16, 24 and 36 h, respectively. (d) α-FeOOH(P-II)/$BiVO_4$ prepared in various pH of 0.02 M $FeCl_2$ solution for 24 h.

PEC performance of as-prepared α-FeOOH/$BiVO_4$ photoanodes were evaluated in

0.2 M Na_2SO_4 under AM 1.5G simulated solar light (100 mW cm^{-2}). In Figure 3a, pristine $BiVO_4$ shows a photocurrent density of 0.35 mA cm^{-2} at 1.23 V *vs.* RHE with an onset potential of around 0.8 V *vs.* RHE. After loading α-FeOOH cocatalyst on $BiVO_4$ films, the photocurrent densities of three photoanodes are increased dramatically and obvious cathodic shifts of the onset potential are observed. The results reveal that the immobilization of α-FeOOH cocatalysts indeed promote the water oxidation activity of the $BiVO_4$ photoanode, consistent with the reported that amorphous FeOOH could improve the photoactivity of $BiVO_4$ photoanode.[35] Surprisingly, the crystalline α-FeOOH(P-II)/$BiVO_4$ displays a remarkable photocurrent density of 2.64 mA cm^{-2} at 1.23 V *vs.* RHE, which is nearly 1.5-fold higher than that of amorphous FeOOH(P-III)/$BiVO_4$ photoanode (1.84 mA cm^{-2}), and even 8-fold higher than that of pristine $BiVO_4$ (0.35 mA cm^{-2}). The performance of α-FeOOH(P-II/III)/$BiVO_4$ (1.97 mA cm^{-2}) is between the crystalline α-FeOOH(P-II)/$BiVO_4$ and amorphouse FeOOH(P-III)/$BiVO_4$ photoanodes. These findings imply that the crystalline α-FeOOH(P-II)/$BiVO_4$ photoanode obtained by $FeCl_2$ as Fe precursor at pH value of 3.42, exhibits the best PEC performance for solar water splitting. In order to find out the underlying mechanism of the dramatic improvement of PEC activity, UV-vis spectra of the pristine $BiVO_4$ and various α-FeOOH cocatalysts modified $BiVO_4$ photoanodes were tested. In Figure 3b, the prepared $BiVO_4$ presents visible-light absorption with the absorption edge at *ca.* 510 nm, which is consistent with the reported $BiVO_4$ with a band gap of 2.4-2.5 eV.[11,36] All the α-FeOOH/$BiVO_4$ photoanodes exhibit similar light absorption spectra, indicating that the influence of light absorption on the photocurrent density is

negligible. Overall, testing results illustrate that the light absorption plays a minor role in the improvement of PEC activity, the best performance of the as-obtained α-FeOOH(P-II)/$BiVO_4$ photoanode could be attributed to the highly crystallized α-FeOOH.

Considering that the preparation time and pH value of $FeCl_x$ solution play important roles on the growth of α-FeOOH crystal, PEC performances of different α-FeOOH/$BiVO_4$ photoanodes obtained in different $FeCl_x$ solutions with various pH values and reaction times were also investigated to optimize the preparation condition of photoanodes. According to *J-V* curves in Figure 3c and Figure 3d, the pH value of 3.42 and preparation time of 24 h were chosen as the optimum conditions for further testing. Meanwhile, the optimized preparation condition of other α-FeOOH/$BiVO_4$ photoanodes were also selected and presented in Figure S2. The photocurrent densities of those photoanodes at 1.23 V *vs.* RHE are shown in Table S2. These findings suggest that no matter which solution was selected, the best PEC performance was obtained on the α-FeOOH/$BiVO_4$ photoanodes prepared in $FeCl_x$ solution with the pH value of 3.42 for 24 hours. Remarkably, the maximum photocurrent density has been obtained using the crystalline α-FeOOH(P-II)/$BiVO_4$ photoanode, which is much higher than those of both amorphous α-FeOOH(P-II/III)/$BiVO_4$ and α-FeOOH(P-III)/$BiVO_4$.

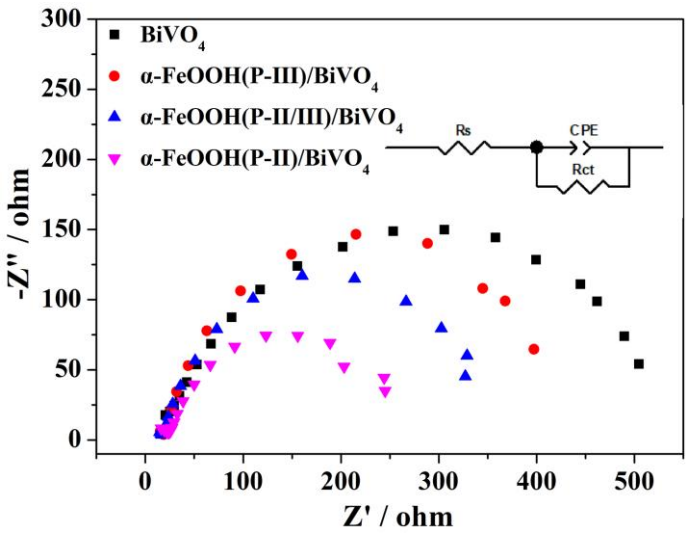

Figure 4. EIS curves of $BiVO_4$, α-FeOOH(P-III)/$BiVO_4$, α-FeOOH(P-II/III)/$BiVO_4$ and α-FeOOH(P-II)/$BiVO_4$ (inset: equivalent circuit).

To gain further insight into the kinetics of solar-driven PEC water splitting process over α-FeOOH/$BiVO_4$ photoanodes, electrochemical impedance spectroscopy (EIS) measurements of all the photoanodes were carried out under AM 1.5 light illumination, and the results were fitted according to the equivalent circuit model (Figure 4). R_s is the system resistance, and R_{ct} represents the charge transfer resistance. According to the fitting results (Table S3), the obtained α-FeOOH/$BiVO_4$ photoanodes have remarkably reduced R_{ct}, compared with pristine $BiVO_4$. Meanwhile, the smallest charge transfer resistance (257.3 Ω) at α-FeOOH(P-II)/$BiVO_4$ indicates that the highly crystallized α-FeOOH provides an efficient pathway for facilitating the charge carrier separation and water oxidation reaction, achieving a remarkable photocurrent density.[37,38]

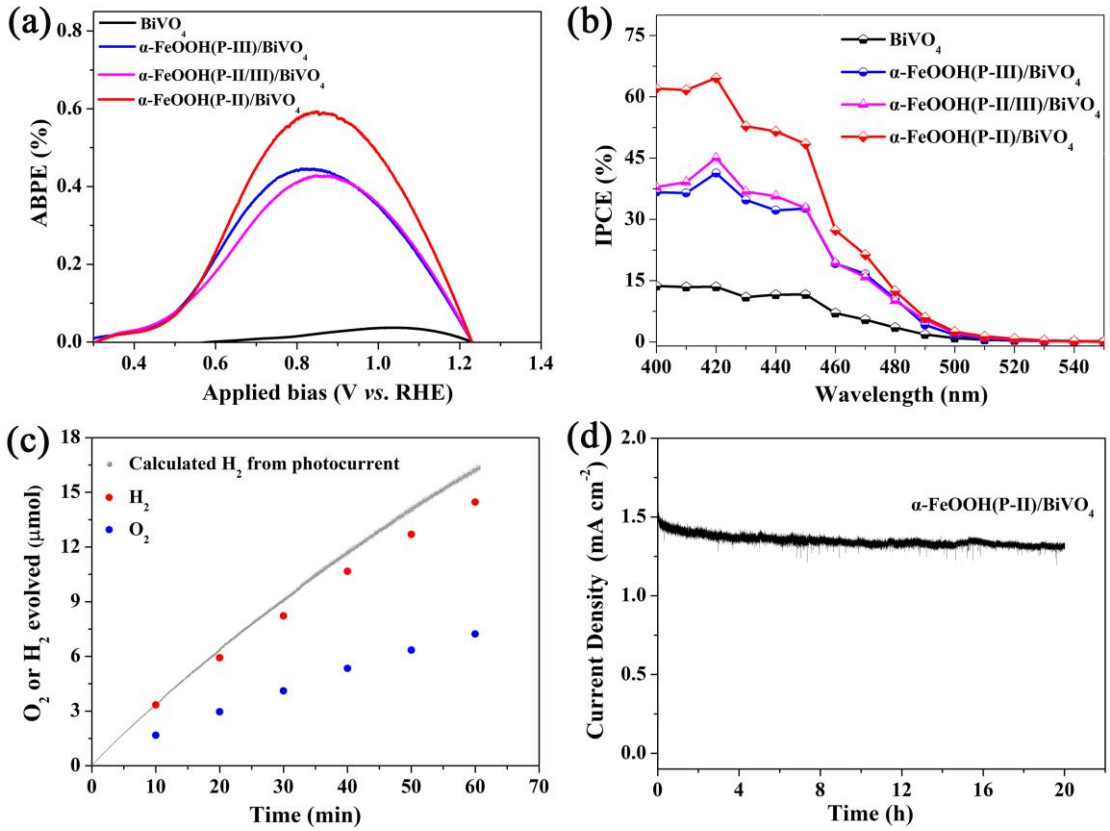

Figure 5. (a) ABPE and (b) IPCE of $BiVO_4$, α-FeOOH(P-III)/$BiVO_4$, α-FeOOH(P-II/III)/$BiVO_4$ and α-FeOOH(P-II)/$BiVO_4$ photoanodes. IPCE measured over the wavelength range of 400 nm to 550 nm at an applied potential of 1.23 V (*vs*. RHE). (c) Detection of H_2 (red) and O_2 (blue) produced by α-FeOOH(P-II)/$BiVO_4$ at 0.9 V *vs*. counter electrode. Black line represents the amount of H_2 calculated assuming 100% faradaic efficiency. (d) Stability testing of the α-FeOOH(P-II)/$BiVO_4$ photoanode at 0.9 V (*vs*. RHE) for 20 h. Electrolyte: 0.2 M Na_2SO_4 (pH = 7).

To quantitatively evaluate PEC water splitting efficiency, the applied bias photon to current efficiencies (ABPE) of all the photoanodes were calculated by *J*-*V* curves,[39] as displayed in Figure 5a. It is observed that the ABPE value of pure $BiVO_4$ is only 0.028% at 0.9 V *vs*. RHE, whereas the ABPE values of the α-FeOOH(P-II/III)/$BiVO_4$ and α-FeOOH(P-III)/$BiVO_4$ photoanodes reach 0.419% and 0.421%, respectively, which means that the surface modification of α-FeOOH cocatalysts effectively promote the

ABPE. Amazingly, the proposed α-FeOOH(P-II)/$BiVO_4$ photoanode can further boost the ABPE to 0.59%, which is over 21-fold higher than that of pure $BiVO_4$. The excellent photo-conversion efficiency at low potential is highly preferable.[40] These results reveal that the crystalline α-FeOOH(P-II)/$BiVO_4$ is more photoactive than amorphous α-FeOOH(P-III)/$BiVO_4$ for OER. Furthermore, the incident photon to current conversion efficiencies (IPCE) of different photoanodes were analyzed by measuring the photocurrent under monochromatic light at 1.23 V *vs.* RHE, as shown in Figure 5b. Over the entire photocurrent responsive region of 400-520 nm, all the α-FeOOH/$BiVO_4$ photoanodes exhibit the similar profiles to the pure $BiVO_4$, consistent with the UV-vis absorption spectra (Figure 3b), revealing that the primary photo-response comes from the $BiVO_4$ rather than α-FeOOH. IPCE of bare $BiVO_4$ is 14.7% (420 nm), similar to the reported value,[21,41] whereas the prepared α-FeOOH(P-II)/$BiVO_4$ photoanode in this work presents a marked improvement and near 5-fold enhancement. Apparently, chemical bath deposition of α-FeOOH is able to create an adequate junction onto $BiVO_4$, which improves the kinetics for water oxidation and suppresses surface recombination of photocarries, through its function as a surface cocatalyst. Overall, at 420 nm, the order of IPCE is α-FeOOH(P-II)/$BiVO_4$ (62.7%) > α-FeOOH(P-II/III)/$BiVO_4$ (45.2%) > α-FeOOH(P-III)/$BiVO_4$ (43.6%) > $BiVO_4$ (14.7%), demonstrating that the well-crystallized α-FeOOH can indeed improve the electron injection efficiency, so more efficient than the low-crystallized/amorphous counterparts. Thus, the superior solar-to-current conversion performance for PEC water oxidation of α-FeOOH(P-II)/$BiVO_4$ is mainly attributed to the highly crystallinity of α-FeOOH.

H_2 and O_2 evolution were then measured using a two-electrode system in an airtight single cell with a bias of 0.9 V in 0.2 M Na_2SO_4 solution (pH = 7). As seen from Figure 5c, the α-FeOOH(P-II)/$BiVO_4$ photoanode continuously produces H_2 (14.5 μmol) and O_2 (7.2 μmol) for 60 min. The produced amount of H_2 and O_2 presents a stoichiometric ratio of 2:1. The corresponding faradaic efficiency of the α-FeOOH(P-II)/$BiVO_4$ photoanode was calculated to be ~92%, revealing that the produced photocurrent can be efficiently utilized to generate H_2 and O_2. 8% difference might be due to the reverse reaction of water splitting as both H_2 and O_2 were produced in a single cell.

In terms of practical application, long-term operational stability of photoelectrodes is highly required, which is also one of the advantages of the crystallized α-FeOOH electrocatalyst.[25] Therefore, the stability of α-FeOOH(P-II)/$BiVO_4$ photoanode for PEC water splitting was tested by a long time run (Figure 5d). Remarkably, stable photocurrent density of α-FeOOH(P-II)/$BiVO_4$ can be observed for 20 hours and no sign of decay is visible, which proves an excellent stability for PEC water oxidation, being consistent with our hypothesis. Moreover, the composition of α-FeOOH(P-II)/$BiVO_4$ before and after 20 hours PEC test was also compared by XPS spectra of Fe2p and O1s (Figure 6). It is clear that XPS spectra of the well-crystallized α-FeOOH(P-II)/$BiVO_4$ remain unchanged after such long time run, further indicating its excellent stability.

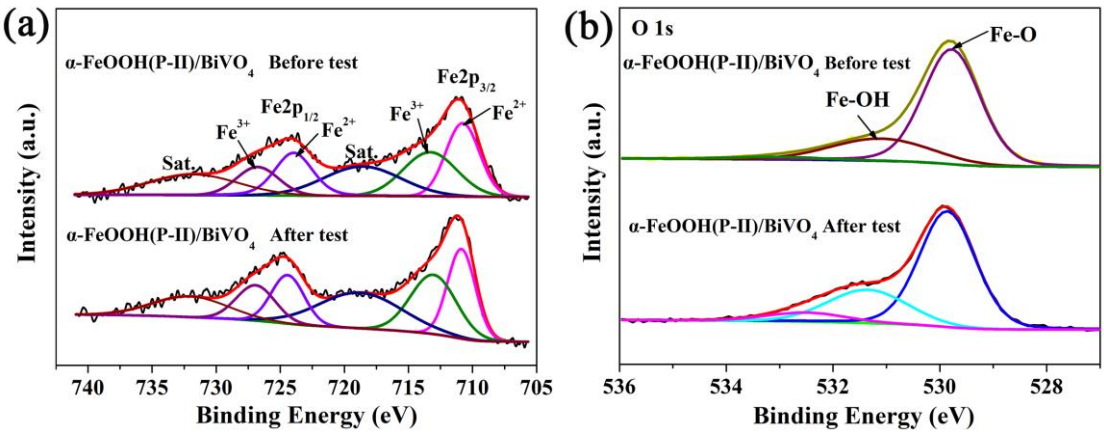

Figure 6. XPS high-resolution of (a) Fe 2p and (b) O 1s spectra of α-FeOOH(P-II)/$BiVO_4$ photoanode before and after 20 hours test.

On the basis of above results, the PEC water splitting by α-FeOOH(P-II)/$BiVO_4$ is summarized in Scheme 2. Under illumination, photogenerated electron-hole pairs are generated by $BiVO_4$. The photogenerated holes can be efficiently transferred from the VB of $BiVO_4$ to the α-FeOOH layer owing to the well-crystallized α-FeOOH interfaces matching well with $BiVO_4$, which could facilitate the hole trapping and migration.[22] During the water oxidation process, the Fe^{3+} is reduced to Fe^{2+} by obtaining electrons from H_2O to produce O_2. Furthermore, owing to the photoholes with high oxidation capacity, the Fe^{3+} can be regenerated by photohole oxidation of Fe^{2+}. Simultaneously, the electrons are transported to the Pt cathode for H_2 generation.

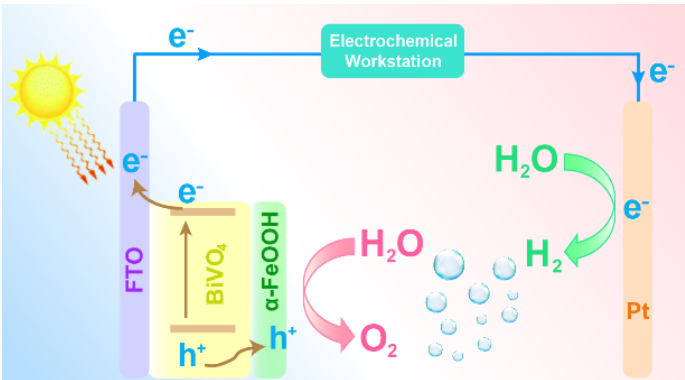

Scheme 2. Illustration of charge separation and transfer in the α-FeOOH(P-II)/$BiVO_4$ photoanode during PEC water splitting.

■ CONCLUSIONS

In summary, a well-crystallized and amorphous α-FeOOH was successfully immobilized on the surface of $BiVO_4$ photoanodes through a reproducible chemical bath deposition method. We found out that Fe precursor, pH value and reaction time were crucial for preparation of the well-crystallized α-FeOOH. As reported, all α-FeOOH improved the PEC performance of $BiVO_4$ photoanodes for water splitting, and the sample of α-FeOOH(P-II)/$BiVO_4$ shows the best performance. The remarkable high performance of the well-crystallized α-FeOOH(P-II)/$BiVO_4$ photoanode remained steady over 20 hours. A 92% faradaic efficiency and the 2:1 H_2 to O_2 ratio also proved the nature of the high PEC performance, which is due to water splitting for H_2 fuel production. Finally, we found that $BiVO_4$ film exhibited an ABPE value of only 0.028% at 0.9 V *vs.* RHE while crystalline α-FeOOH(P-II)/$BiVO_4$ photoanode represented an ABPE to 0.59% under same condition, more than 21 times higher compared with the $BiVO_4$ photoanode. Based on the characterizations of XRD, HRTEM and XPS, the performance of the as-obtained α-FeOOH(P-II)/$BiVO_4$ photoanodes could be related to the crystallinity of α-FeOOH. Further analysis of EIS indicates effective charge carrier separation and transfer was facilitated by the well-crystallized α-FeOOH. All these resulted into the best photoanode of the crystalline α-FeOOH(P-II)/$BiVO_4$. The new findings will pave the way toward economically viable, efficient and stable cocatalysts for photoelectrochemical water splitting.

■ ASSOCIATED CONTENT

Supporting Information.

The Supporting information is available free of charge

Experimental section, HRTEM, J-V curves and photocurrent densities of samples prepared at different pH and under different reaction conditions, ICP-MS analysis and EIS data.

■ AUTHOR INFORMATION

Corresponding Author

Hai-Ying Jiang- *Key Laboratory of Synthetic and Natural Functional Molecule of the Ministry of Education, The Energy and Catalysis Hub, College of Chemistry and Materials Science, Northwest University, Xi'an 710127, P. R. China.* E-mail: jianghy@nwu.edu.cn

Junwang Tang-*Department of Chemical Engineering, University College London, Torrington Place, London WC1E 7JE, U.K.* orcid.org/0000-0002-2323-5510; E-mail: junwang.tang@ucl.ac.uk

Notes

The authors declare no competing financial interest.

■ ACKNOWLEDGMENTS

W. Z and H.-Y. J. are grateful for the financial supports of this work from Supported by National Natural Science Foundation of China (No. 21703170). L. Q. X. and J. W. T. are thankful for financial support from UK EPSRC (EP/N009533/1), RS

International Exchanges 2017 Cost Share Award (IEC\NSFC\170342), Royal Society-Newton Advanced Fellowship grant (NA170422) and the Leverhulme Trust (RPG-2017-122).

■ REFERENCES

(1) Choi, D.; Nam, S. K.; Kim, L.; Moon, J. H. Enhanced Photoelectrochemical Water Splitting Through Bismuth Vanadate with A Photon Upconversion Luminescent Reflector. *Angew. Chem. Int. Ed.* **2019**, 58, 6891–6895.

(2) Li, Z. S.; Luo, W. J.; Zhang, M. L.; Feng, J. Y.; Zou, Z. G. Photoelectrochemical Cells for Solar Hydrogen Production: Current State of Promising Photoelectrodes, Methods to Improve their Properties, and Outlook. *Energy Environ. Sci.* **2013**, 6, 347–370.

(3) Zhang, H. P.; Wang, Z. Y.; Huang, B. B. Fabrication of $BiVO_4$ Photoanode Consisted of Mesoporous Nanoparticles with Improved Bulk Charge Separation Efficiency. *Appl. Catal. B: Environ.* **2018**, *238*, 586–591.

(4) Kim, J. H.; Lee, J. S. Elaborately Modified $BiVO_4$ Photoanodes for Solar Water Splitting. *Adv. Mater.* **2019**, *31*, 1806938.

(5) Moniz, S. J. A.; Zhu, J.; Tang, J. W. 1D Co-Pi Modified $BiVO_4$/ZnO Junction Cascade for Efficient Photoelectrochemical Water Cleavage. *Adv. Energy Mater.* **2014**, *4*, 1301590.

(6) Chen, S. Y.; Yang, J. S.; Wu, J. J. Three-Dimensional Undoped Crystalline SnO_2 Nanodendrite Arrays Enable Efficient Charge Separation in $BiVO_4$/SnO_2 Heterojunction Photoanodes for Photoelectrochemical Water Splitting. *ACS Appl. Energy Mater.* **2018**, *1*, 2143−2149.

(7) Tan, H. L.; Wen, X. M.; Amal, R.; Ng, Y. H. $BiVO_4$ {010} and {110} Relative Exposure Extent: Governing Factor of Surface Charge Population and Photocatalytic Activity. *J. Phys. Chem. Lett.* **2016**, *7*, 1400−1405.

(8) Wang, S. C.; He, T. W.; Yun, J. H.; Hu, Y. X.; Xiao, M.; Du, A. J.; Wang, L. Z. New Iron-Cobalt Oxide Catalysts Promoting $BiVO_4$ Films for Photoelectrochemical Water Splitting. *Adv. Funct. Mater.* **2018**, *28*, 1802685.

(9) Jian, J.; Xu, Y. X.; Yang, X. K.; Jia, L. C.; Friedrich, D.; van de Krol, R.; Wang, H. Q. Embedding Laser Generated Nanocrystals in $BiVO_4$ Photoanode for Efficient Photoelectrochemical Water Splitting. *Nat. Commun.* **2019**, *10*, 2609.

(10) Wang, R. R.; Luo, L.; Zhu, X. L.; Yan, Y.; Zhang, B.; Xiang, X.; He, J. Plasmon-Enhanced Layered Double Hydroxide Composite $BiVO_4$ Photoanodes: Layering-Dependent Modulation of the Water Oxidation Reaction. *ACS Appl. Energy Mater.* **2018**, *1*, 3577−3586.

(11) Xia, L. G.; Bai, J.; Li, J. H.; Zeng, Q. Y.; Li, L. S.; Zhou, B. X. High-Performance $BiVO_4$ Photoanodes Cocatalyzed with an Ultrathin α-Fe_2O_3 Layer for Photoelectrochemical Application. *Appl. Catal. B: Environ.* **2017**, *204*, 127–133.

(12) Malara, F.; Fabbri, F.; Marelli, M.; Naldoni, A. Controlling the Surface Energetics and Kinetics of Hematite Photoanodes through Few Atomic Layers of NiO_x. *ACS Catal.* **2016**, *6*, 3619–3628.

(13) Lei, F.; Sun, Y.; Liu, K.; Gao, S.; Liang, L.; Pan, B.; Xie, Y. Oxygen Vacancies Confined in Ultrathin Indium Oxide Porous Sheets for Promoted Visible-Light Water Splitting. *J. Am. Chem. Soc.* **2014**, *136*, 6826–6829.

(14) Wang, S. C.; Liu, G.; Wang, L. Z. Crystal Facet Engineering of Photoelectrodes for Photoelectrochemical Water Splitting. *Chem. Rev.* **2019**, *119*, 5192–5247.

(15) She, H. D.; Yue, P. F.; Ma, X. Y.; Huang, J. W.; Wang, L.; Wang, Q. Z. Fabrication of $BiVO_4$ Photoanode Cocatalyzed with NiCo-layered Double Hydroxide for Enhanced Photoactivity of Water Oxidation. *Appl. Catal. B: Environ.* **2020**, *263*, 118280.

(16) García-Tecedor, M.; Cardenas-Morcoso, D.; Fernández-Climent, R.; Giménez, S. The Role of Underlayers and Overlayers in Thin Film $BiVO_4$ Photoanodes for Solar Water Splitting. *Adv. Mater. Interfaces* **2019**, *6*, 1900299.

(17) Ho-Kimura, S.; Moniz, S. J. A.; Handoko, A. D.; Tang, J. W. Enhanced Photoelectrochemical Water Splitting by Nanostructured $BiVO_4$-TiO_2 Composite Electrodes. *J. Mater. Chem. A* **2014**, *2*, 3948–3953.

(18) Singh, A. P.; Sainia, N.; Mehta, B. R.; Hellman, A.; Iandolo, B.; Wickman, B. Hydrogen Treatment and FeOOH Overlayer: Effective Approaches for Enhancing the Photoelectrochemical Water Oxidation Performance of Bismuth Vanadate Thin Films. *Catal. Today* 2019, 321-322, 87–93.

(19) Ye, K. H.; Wang, Z. L.; Gu, J. W.; Xiao, S.; Yuan, Y. F.; Zhu, Y.; Zhang, Y. M.; Mai, W. J.; Yang, S. H. Carbon Quantum Dots as a Visible Light Sensitizer to Significantly Increase the Solar Water Splitting Performance of Bismuth Vanadate Photoanodes. *Energy Environ. Sci.* **2017**, *10*, 772–779.

(20) Arunachalam, M.; Ahn, K. S.; Kang, S. H. Oxygen Evolution NiOOH Catalyst Assisted V_2O_5@$BiVO_4$ Inverse Opal Hetero-Structure for Solar Water Oxidation. *Int. J. Hydrogen Energy* **2019**, *44*, 4656–4663.

(21) Zhang, B. B.; Huang, X. J.; Hu, H. Y.; Chou, L. J.; Bi, Y. P. Defect-Rich and Ultrathin CoOOH Nanolayers as Highly Efficient Oxygen Evolution Catalysts for Photoelectrochemical Water Splitting. *J. Mater. Chem. A* **2019**, *7*, 4415–4419.

(22) Kim, T. W.; Choi, K. S. Nanoporous $BiVO_4$ Photoanodes with Dual-Layer Oxygen Evolution Catalysts for Solar Water Splitting. *Science* **2014**, *343*, 990–994.

(23) Burke, M. S.; Kast, M. G.; Trotochaud, L.; Smith, A. M.; Boettcher, S. W. Cobalt–Iron (oxy)hydroxide Oxygen Evolution Electrocatalysts: The Role of Structure and Composition on Activity, Stability, and Mechanism. *J. Am. Chem. Soc.* **2015**, *137*, 3638–3648.

(24) Chemelewski, W. D.; Rosenstock, J. R.; Mullins, C. B. Electrodeposition of Ni-doped FeOOH Oxygen Evolution Reaction Catalyst for Photoelectrochemical Water Splitting. *J. Mater. Chem. A* **2014**, *2*, 14957–14962.

(25) Lee, D. K.; Choi, K. S. Enhancing Long-Term Photostability of $BiVO_4$ Photoanodes for Solar Water Splitting by Tuning Electrolyte Composition. *Nat. Energy* **2018**, *3*, 53–60.

(26) Hu, C. W.; Yamada, Y.; Yoshimura, K. Fabrication of nickel oxyhydroxide/palladium(NiOOH/Pd) thin films for gasochromic application. *J. Mater. Chem. C*, **2016**, *4*, 5390.

(27) Li, Z. H.; Feng, S. L.; Liu, S. Y.; Li, X.; Wang, L.; Lu, W. Q. A three-dimensional interconnected hierarchical FeOOH/TiO2/ZnO nanostructural photoanode for enhancing the performance of photoelectrochemical water oxidatio. *Nanoscale*, **2015**, *7*, 19178.

(28) Luo, W. J.; Jiang, C. R.; Li, Y. M.; Shevlin, S. A.; Han, X. Y.; Qiu, K. P.; Cheng, Y. C.; Guo, Z. X.; Huang, W.; Tang, J. W. Highly Crystallized α-FeOOH for a Stable and Efficient Oxygen Evolution Reaction. *J. Mater. Chem. A* **2017**, *5*, 2021–2028.

(29) Zhang, Y. X.; Jia, Y. A Facile Solution Approach for the Synthesis of Akaganéite (β-FeOOH) Nanorods and their Ion-Exchange Mechanism toward As(V) Ions. *Appl. Surf. Sci.* **2014**, *290*, 102–106.

(30) Yan, J. Q.; Li, P.; Ji, Y. J.; Bian, H.; Li, Y. Y.; (Frank) Liu, S. Z. Earth-Abundant Elements Doping for Robust and Stable Solar-Driven Water Splitting by FeOOH. *J. Mater. Chem. A* **2017**, *5*, 21478–21485.

(31) Zhan, F. Q.; Yang, Y. H.; Liu, W. H.; Wang, K. K.; Li, W. Z.; Li, J. Facile Synthesis of FeOOH Quantum Dots Modified ZnO Nanorods Films via a Metal-Solating Process. *ACS Sustainable Chem. Eng.* **2018,** *6*, 7789–7798.

(32) Wang, L.; Yang, Y.; Zhang, Y. J.; Rui, Q.; Zhang, B. B.; Shen, Z. Q.; Bi, Y. P. One-Dimensional Hematite Photoanodes with Spatially Separated Pt and FeOOH Nanolayers for Efficient Solar Water Splitting. *J. Mater. Chem. A* **2017,** *5*, 17056–17063.

(33) Park, G.; Kim, Y.; Kim, Y. H.; Park, M.; Song, H.; Nam, K. M. Preparation and Phase Transition of FeOOH Nanorods: Strain Effects on Catalytic Water Oxidation. *Nanoscale* **2017,** *9*, 4751–4758.

(34) Liu, C.; Zhou, J. L.; Su, J. Z.; Guo, L. J. Turning the Unwanted Surface Bismuth Enrichment to Favourable $BiVO_4$/BiOCl Heterojunction for Enhanced Photoelectrochemical Performance. *Appl. Catal. B: Environ.* **2019**, *241*, 506–513.

(35) Kim, J. Y.; Youn, D. H.; Kang, K.; Lee, J. S. Highly Conformal Deposition of an Ultrathin FeOOH Layer on a Hematite Nanostructure for Efficient Solar Water Splitting. *Angew. Chem. Int. Ed.* **2016,** *55*, 10854–10858.

(36) Tan, H. L.; Abdi, F. F.; Ng, Y. H. Heterogeneous Photocatalysts: An Overview of Classic and Modern Approaches for Optical, Electronic, and Charge Dynamics Evaluation. *Chem. Soc. Rev.* **2019**, *48*, 1255–1271.

(37) Chong, R. F.; Du, Y. Q.; Chang, Z. X.; Jia, Y. S.; Qiao, Y.; Liu, S. H.; Liu, Y.; Zhou, Y. M.; Li, D. L. 2D Co-Incorporated Hydroxyapatite Nanoarchitecture as a Potential Efficient Oxygen Evolution Cocatalyst for Boosting Photoelectrochemical Water Splitting on Fe_2O_3 Photoanode. *Appl. Catal. B: Environ.* **2019**, *250*, 224–233.

(38) Xie, Z. R.; Tan, H. L.; Wen, X. M.; Suzuki, Y.; Iwase, A.; Kudo, A.; Amal, R.; Scott, J.; Ng. Y. H. The Importance of the Interfacial Contact: Is Reduced Graphene Oxide Always an Enhancer in Photo(Electro)Catalytic Water Oxidation? *ACS Appl. Mater. Interfaces* **2019**, *11*, 23125–23134.

(39) Walter, M. G.; Warren, E. L.; McKone, J. R.; Boettcher, S. W.; Mi, Q. X.; Santori, E. A.; Lewis, N. S. Solar Water Splitting Cells. *Chem. Rev.* **2010**, *110*, 6446.

(40) Vo, T. G.; Chiu, J. M.; Tai, Y.; Chiang, C. Y. Turnip-Inspired $BiVO_4$/CuSCN Nanostructure with Close to 100% Suppression of Surface Recombination for Solar Water Splitting. *Sol. Energy Mater. Sol. Cells* **2018**, *185*, 415–424.

(41) Pan, Q. G.; Zhang, C.; Xiong, Y. J.; Mi, Q. X.; Li, D. D.; Zou, L. L.; Huang, Q. H.; Zou, Z.; Yang, Q. H. Boosting Charge Separation and Transfer by Plasmon-Enhanced MoS_2/$BiVO_4$ p-n Heterojunction Composite for Efficient Photoelectrochemical Water Splitting. *ACS Sustainable Chem. Eng.* **2018**, *6*, 6378–6387.

For Table of Contents Only